PAPER • **OPEN ACCESS**

Simulation of atom trajectories in the original Stern–Gerlach experiment

To cite this article: Faraz Mostafaeipour *et al* 2025 *Phys. Scr.* **100** 045410

Physica Scripta

PAPER

Simulation of atom trajectories in the original Stern–Gerlach experiment

Faraz Mostafaeipour[1,2,3], **S Süleyman Kahraman**[2,3], **Kelvin Titimbo**[2,3], **Yixuan Tan**[2] and **Lihong V Wang**[2]

[1] Division of Physics, Mathematics and Astronomy, California Institute of Technology, Pasadena, CA 91125, United States of America
[2] Caltech Optical Imaging Laboratory, Andrew and Peggy Cherng Department of Medical Engineering, Department of Electrical Engineering, California Institute of Technology, 1200 E. California Blvd., MC 138-78, Pasadena, CA 91125, United States of America
[3] These authors contributed equally.

E-mail: lvw@caltech.edu

Keywords: Stern–Gerlach experiment, semiclassical theory, spin measurement

OPEN ACCESS

RECEIVED
10 September 2024

REVISED
3 March 2025

ACCEPTED FOR PUBLICATION
11 March 2025

PUBLISHED
27 March 2025

Abstract

Following a comprehensive analysis of the historical literature, we model the geometry of the Stern–Gerlach experiment to numerically calculate the magnetic field using the finite-element method. Using this calculated field and Monte Carlo methods, the semiclassical atomic translational dynamics are simulated to produce the well-known quantized end-pattern with matching dimensions. The finite-element method used provides the most accurate description of the Stern–Gerlach magnetic field and end-pattern in the literature, matching the historically reported values and figures.

1. Introduction

In 1922, Otto Stern and Walther Gerlach reported what is now known as the Stern–Gerlach experiment (SGE), a fundamental milestone in the development of modern physics [1–3]. Following Stern's preliminary work on the kinetic theory of gases and molecular beams [4, 5], the SGE is a significant benchmark as it presented direct proof for angular momentum quantization [6, 7], confirmed the electron intrinsic spin years later [8], allowed for the selection of spin-polarized atoms, is the first measurement of atomic ground state properties without electronic excitation, and led to further research into entanglement, non-classical correlations, and the measurement problem [9, 10]. As a result, the SGE has been widely used as an introduction to quantum theory in contemporary textbooks [11–13].

The three-paper series [1–3] described the deflection of a beam of silver atoms as it traversed a region with an inhomogeneous magnetic field **B**. The first of the series set out the preliminary framework, showing experimental proof of the silver atom's magnetic moment [1]. A few months later, in the second paper of the series, they published experimental verification of directional quantization, producing the well-known splitting patterns seen in figure 1(a) [2]. In the third publication, they improved the precision of their measurements by addressing uncertainties related to the atomic beam's distance from the magnet and the strength of the magnetic field. Maintaining the same experimental apparatus, they measured 'the magnetic moment of the normal silver atom in the gaseous state [as] a Bohr magneton' [3, 14].

Figure 2(a) shows a model of the original SGE. Heated silver atoms effuse from the oven (O), predominantly propagating along the y-direction. The atoms travel through two collimating apertures (A1 and A2), pass through an inhomogeneous magnetic field gradient generated by two ferromagnetic pole-pieces, and ultimately deposit on the detector plate (D). The experiment reveals the splitting of the beam into two components along the z direction. As shown in figures 2(a)–(b), the upper magnet consists of a blade-shaped pole and the lower magnet is characterized by its furrowed shape, commonly referred to as the cutting edge (CE) and the trench (T), respectively. Angular splitting occurs maximally at the center of the magnet along the x-direction and decreases progressively towards the sides, as depicted in figures 1(a)–(b).

In this work, we present an accurate model of the Stern–Gerlach experiment using the COMSOL Multiphysics® finite element analysis tool. This approach refines the approximations used in many prior studies,

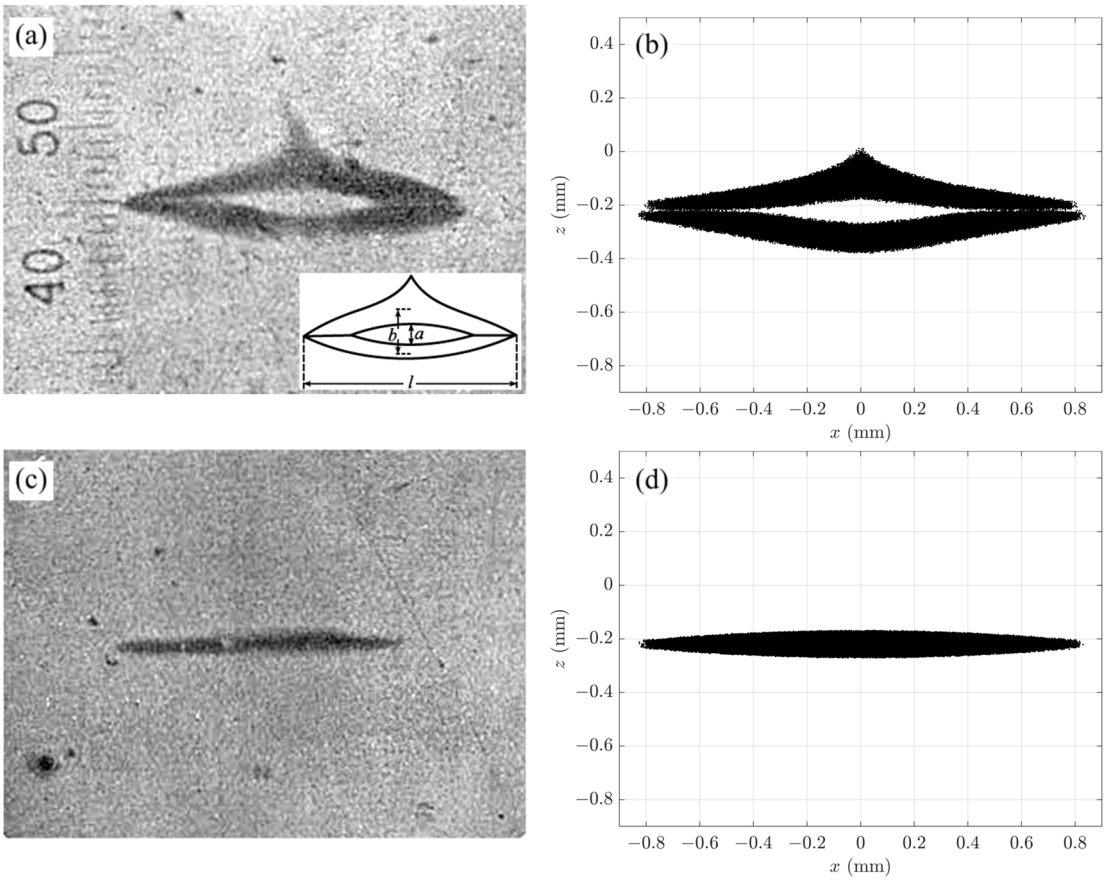

Figure 1. Detected end-patterns for $\mathbf{B} \neq 0$ (top) and $\mathbf{B} = 0$ (bottom). Panels (a) and (c) depict the original patterns reported by Stern and Gerlach [2]. Panels (b) and (d) present the corresponding simulation results. Inset in (a) provides a representative illustration of the pattern displaying its length and width attributes reported in [2]. Note that both patterns are to scale. Reproduced from [2], with permission from Springer Nature.

which often model the magnetic field analytically with simplified assumptions, such as a spatially linear field dependence [15–18]. The field is sometimes simplified into only a gradient along the quantization axis by only solving for a subset of the space [19], or by assuming that the force along the other dimension averages to zero due to rapid precession [20–22]. While such approximations offer valuable insights, they do not always fully conform to Maxwell's equations for static fields and may oversimplify the actual field geometry. Additionally, we conduct a classical Monte Carlo simulation of the atomic trajectories through the accurately modeled field. In the classical simulation of the trajectories, we assume each atom can occupy one of two discrete states, with the magnetic moment being either parallel or anti-parallel to the z-direction. This assumption is inspired by quantum mechanics, where spin measurements along a given axis yield binary outcomes. However, no explicit mechanism for the reduction of the spin wave function is assumed here; rather, the two-state treatment serves as a simplification for modeling the experiment. To the best of our knowledge, this work provides the most precise numerical replication to date of both the original magnetic field and the end-pattern observed in the historical SGE, providing a valuable complement to the existing literature [23, 24].

2. Simulation

The field properties and the atomic trajectories are modeled based on the historically accurate features and parameters derived from the original 1922 SGE papers [1–3] and subsequent review studies [10, 14, 25, 26].

2.1. Modeling the magnetic field

Finite-element analysis is used to calculate the magnetic field $\mathbf{B} = (B_x, B_y, B_z)$ via COMSOL Multiphysics® [27]. The three-dimensional geometry of the magnets have been meticulously reconstructed and matched as closely as possible to those in the references. In COMSOL, a high-resolution `extremely fine mesh` was selected to enhance the accuracy of the magnetic field gradient.

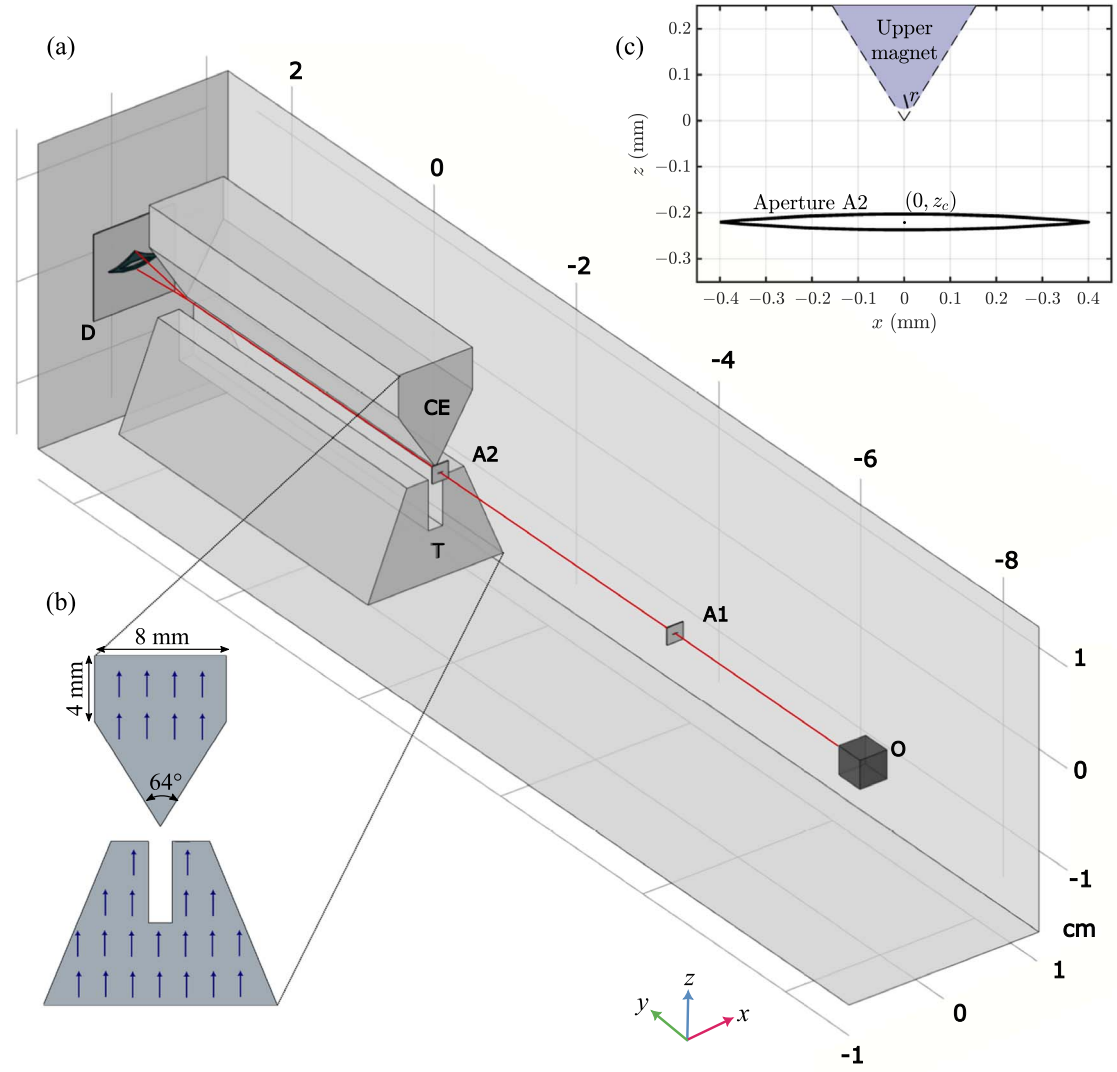

Figure 2. Modelled Stern–Gerlach experiment. (a) Three-dimensional geometry of our model. O: oven. A1 and A2: apertures. CE: magnet cutting edge. T: magnet trench. D: detector. (b) Cross-section of the magnets in the transverse plane. The blue arrows indicate the magnetization direction. (c) Cross-section of Aperture 2 (A2) with a width of $w = 35$ μm and a length of $l = 0.8$ mm. A rounded transition with a radius $r = 30$ μm was applied to smoothen the CE tip.

In figure 2, the reference frame's origin is centered at the middle of the magnets. The magnets, which are 3.5 cm in length, extend along the y-axis from $y = -1.75$ to 1.75 cm. The magnets' cross-section is shown in figure 2(b). The trench of the lower magnet has a depth of 5 mm and a width of 1.5 mm. The CE tip of the upper magnet converges to the point $(x, z) = (0, 0)$, features a wedge angle of 64○, and sits 1 mm above the top of the trench. The described cut-plane geometry is modeled after the experimental schematic presented in the original report [2]. The magnets are assumed to have a relative permeability of $\mu/\mu_0 = 400$, where μ_0 is the vacuum magnetic permeability, and a magnetization of 253 kA/m in the $+z$-direction.

Non-smooth corners can introduce numerical inaccuracies in finite element analysis, particularly in regions of interest where magnetic field gradients are crucial. To mitigate such inaccuracies near the CE tip, we applied a rounded transition with a radius of 30 μm to smooth the corner, as shown in figure 2(c). The precise shape of the CE tip is significant, as its proximity to the atomic trajectories means that any singularity in the magnetic field gradient can result in inaccuracies in the simulated trajectories.

As shown in figure 2(a), the oven O is placed at $y = -7.65$ cm along the propagation direction. A circular aperture, A1, with a diameter of 31 μm, is positioned 2.50 cm away at $y = -5.15$ cm. The original SGE papers describe A2 as a slit-shaped aperture with a length of 0.8 mm and a width of 30–40 μm, positioned 3.35 cm away from A1, directly in front of the SG magnets (at $y = -1.80$ cm). The oven, O, and the apertures, A1 and A2, define the trajectory of the beam, which is centered at $(x, z) = (0, z_c)$ in the transverse plane. Because beam deflection before the magnets is negligible, z_c describes the vertical distance between the CE tip and the atomic beam at the entrance of the magnets (see figure 2(c)). The detector plate D is placed immediately after the

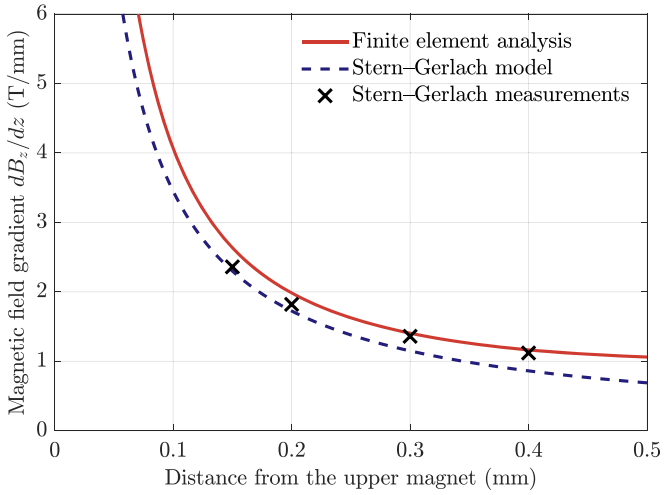

Figure 3. (Red line) Gradient of the magnetic field along the z axis calculated using the finite element method. The same gradient is (blue dashed line) theoretically modeled and (black crosses) experimentally measured by Stern and Gerlach [3].

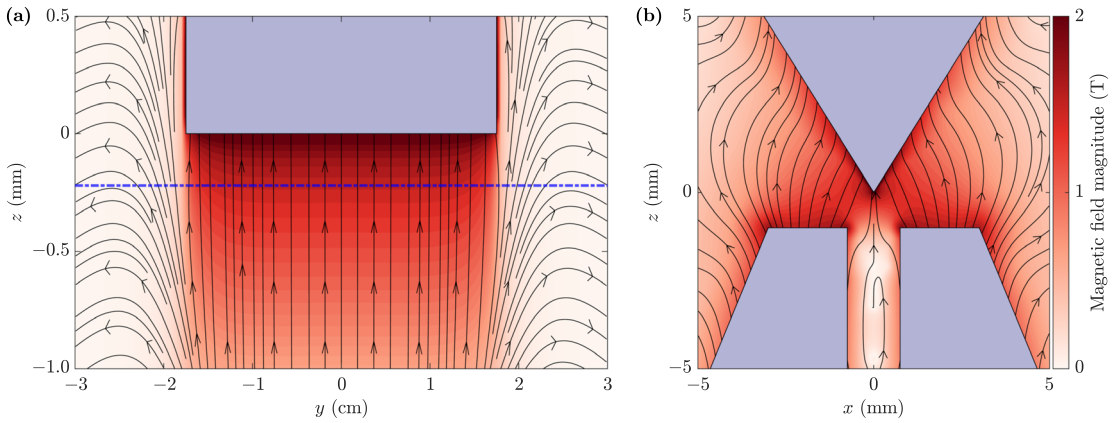

Figure 4. Cross-section of the magnetic field on the (a) yz plane at $x = 0$ and (b) xz plane at $y = 0$. The magnets are in grey, and the magnetic field lines are in black. The blue dashed line indicates the center of the atomic beam, z_c, at the entrance.

magnets at $y = 1.8$ cm. The scale and geometry of the simulation components are calculated in accordance with the literature [2, 14, 25].

In the absence of a magnetic field gradient, it is expected that the shape of the end-pattern on the detector plate is a scaled projection of the A2 shape, as illustrated in figure 1(c). Based on this, and lacking a precise description, we modeled A2 as an eye-shaped aperture [28] to closely approximate the reported zero-field ($\mathbf{B} = 0$) end-pattern length and width [2]. Thus, the contour of the aperture is defined as the intersection of the two parabolae:

$$f_{z,\pm}(x) = \pm\frac{2w}{l^2}x^2 + z_c \mp \frac{w}{2}, \qquad -l/2 \leqslant x \leqslant l/2, \tag{1}$$

with $l = 0.8$ mm and $w = 35$ μm as shown in figure 2(c), and produces the simulated pattern depicted in figure 1(d).

Because there is no reference to the magnitude of the magnetic field that Stern and Gerlach specifically used for the reported pattern, we adjusted the field strength such that $\frac{\partial B_z}{\partial z}$ as a function of z matches the reported experimental values from the third 1922 SGE paper [3]. The theoretical model and experimental measurements of $\frac{\partial B_z}{\partial z}$ presented in [3] closely align with the COMSOL simulations shown in figure 3.

The COMSOL-simulated magnetic field cross-sections on the xz plane at $y = 0$ and the yz plane at $x = 0$ are shown in figure 4. Additionally, the variation of the magnitudes of the magnetic field components along the propagation axis y at the coordinates $(x, z) = (0, z_c = -0.22$ mm) are presented in figure 5. The non-trivial field depicted in the figures is divergence-free up to the numerical accuracy.

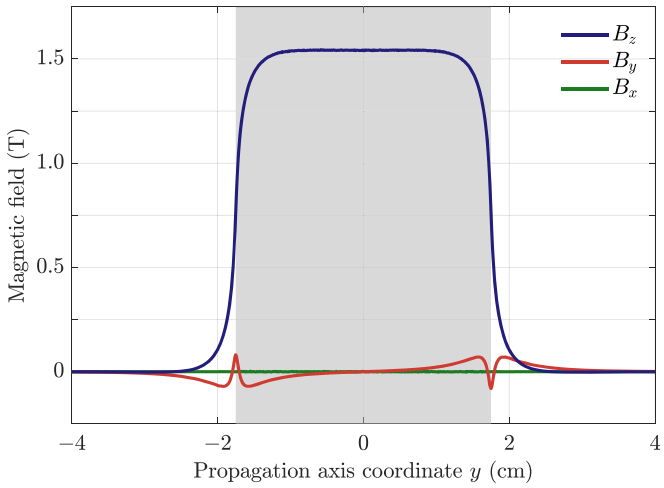

Figure 5. Intensity of the magnetic field components: B_z (blue), B_y (red), and B_x (green) along the propagation axis $(0, y, z_c)$. The shaded area indicates the location of the magnets. Due to symmetry, we have $B_x = 0$. Because $\nabla \cdot \mathbf{B} = 0$, B_y shows small fluctuations near the ends of the magnets.

2.2. Atomic trajectories

A Monte Carlo simulation is calculated where $N = 10^7$ silver atoms (with atomic mass $M = 107.868$ Da) are ejected from the oven's circular aperture with an area of 1 mm^2, populated based on a random radial Gaussian distribution centered at (x, z_c). The atomic translational dynamics are numerically calculated using Euler's method based on the classical equation of motion for the neutral atoms in the experiment:

$$\frac{\mathrm{d}^2\mathbf{r}}{\mathrm{d}t^2} = -\frac{1}{M}\boldsymbol{\nabla}(-\boldsymbol{\mu}_e \cdot \mathbf{B}(\mathbf{r})) \tag{2}$$

where t is time, $\mathbf{r}$ is the position of the atom, $\boldsymbol{\mu}_e$ is the magnetic moment of the electron, $\mathbf{B}(\mathbf{r})$ is the magnetic field at coordinate $\mathbf{r}$. Our simulation code is available online for reference [29].

For simplicity, we assume that the electron magnetic moments are statistically evenly distributed between parallel and anti-parallel orientations relative to the z-axis immediately upon exiting the oven; no magnetic moment is assumed to be oriented at an oblique angle. This assumption is equivalent to solving two independent trajectory equations for each eigenstate for a spin 1/2 [15, 19]. Various descriptions are available in the literature, but solving two independent equations for each state is widely implemented [10, 16, 18, 19, 30]. For comparison, atoms with classical unquantized magnetic moments (sampled from an isotropic distribution) are simulated, yielding an expected continuous end-pattern (see figure A.1 in Appendix A).

The atoms' initial angular distribution of velocities are sampled from within a solid cone spreading outward in the positive y-direction with a vertex angle selected such that it fills A1. The speeds are uniformly sampled in the range $|\overrightarrow{v}| = [625,\ 750]$ m s^{-1}. Details about the velocity selection are further outlined in section 3. After exiting the oven, the atoms travel to the first selecting aperture (A1), and those that pass through continue towards the second aperture (A2). From A2, the atoms traverse through the magnet and hit the detector plate placed immediately after the magnet. As previously mentioned, the oven, apertures, and therefore, the atomic beam are centered at $(x, z) = (0, z_c = -0.22$ mm). This choice is based on the study of different end-patterns as illustrated in figure 6. The simulation does not consider reflections off the magnets and disables particles that interact with the apertures, magnets, and surrounding environment.

An alternative assumption for calculating the trajectories is that the magnetic moment adiabatically follows the local field direction, instead of remaining fixed along the z axis. Since the magnetic field from the main pole pieces varies gradually, with a rotation frequency less than the Larmor frequency, adiabatic evolution is a reasonable assumption, provided there are no additional magnetic field sources along the flight path that could induce non-adiabatic transitions. In Appendix B, we simulate the trajectories under this assumption and present the resulting end-pattern in figure B.1. The results indicate that the final distribution remains largely unchanged compared to the case where spins remain trivially aligned along the z-axis.

3. Discussion

As shown in figure 3, the simulated magnetic field gradients agree with the experimentally reported values in the literature. Additionally, the selection of $z_c = -0.22$ mm ensures that B_z, as seen in figure 5, is close to the

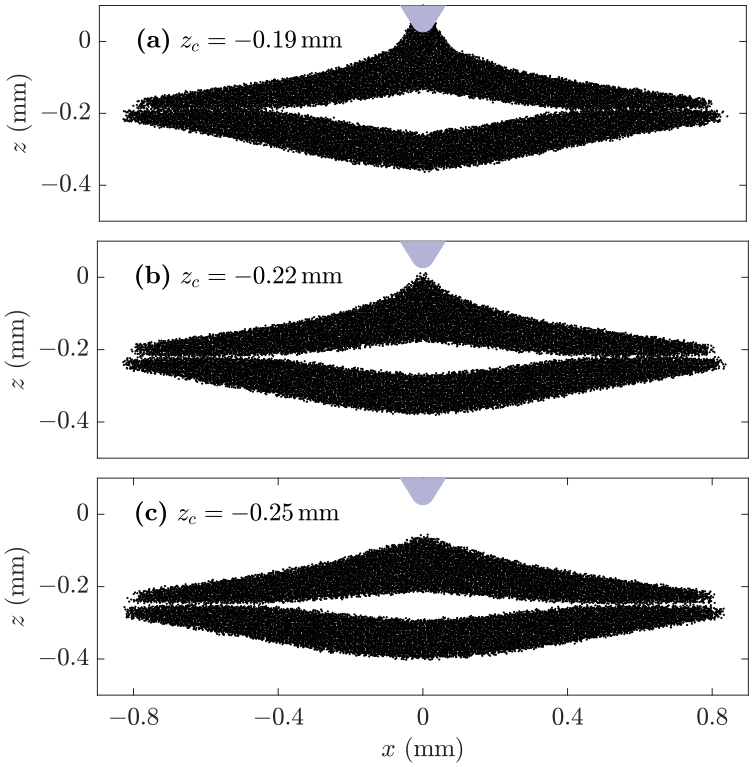

Figure 6. End-patterns for different distances between the apertures and the upper magnet, z_c. Atoms traveling closer to the CE tip of the upper magnet experience stronger field gradients.

magnetic field strength of ~ 1.65 T reported in a later publication by Stern and Gerlach [25]. Moreover, the resulting atomic distribution on the screen replicates the characteristic pattern observed in the original experiment. From the simulations, we find that variations in the trench depth do not alter the magnetic field enough to significantly change the end-patterns. Based on a thorough review of the available literature and the results presented here, this work provides the most detailed and comprehensive numerical reconstruction of the magnetic field used in the original Stern–Gerlach experiment.

As shown in figure 1, Stern and Gerlach measured the minimum splitting $a_{\text{exp}} = 0.11$ mm, the average splitting $b_{\text{exp}} = 0.2$ mm, and the pattern length $L_{\text{exp}} = 1.1$ mm [2]. From the description of the original SGE, several variables, such as z_c and propagation velocities, remain historically unknown and can be tuned within an appropriate range to match the end-pattern in [2].

As the SGE was an experimental consequence of Stern's preliminary work on molecular velocity measurements, the methodology for producing the atomic silver beam is similar. The approach is based on heating a silver wire to its melting point, causing it to evaporate under vacuum, thus creating an isotropic propagation of atoms. This atomic cloud is then collimated into a beam as it passes through a series of consecutive apertures. Placing a cold metal plate along the beam path causes the vapor to condensate on the detector [14]. While the original SGE setup utilized a silver-loaded clay furnace for more stability over time, the fundamental principle of emission remains the same [25, 28]. The melting temperature of silver is 1235 K [31] and the original SGE reports an oven temperature of 1323 K [25]. By using the speed distribution for molecular beams $\left(p(v) = \frac{1}{2}\left(\frac{M}{k_b T}\right)^2 v^3 \exp\left[-\frac{Mv^2}{2k_b T}\right]\right)$ for a given temperature T, we obtain the root-mean-squared speed $v_{\text{rms}} = \sqrt{4k_b T/M}$, where k_b is the Boltzmann constant [4, 5, 32]. The temperature and the corresponding root-mean-squared speed provide a feasible range for the simulated speed distribution.

From our simulation, we found that the maximum and minimum speeds selected from the distribution are correlated to the minimum splitting and average splitting values, respectively. We assume a uniform speed distribution and reverse engineer the bounds within the feasible range to match the observed end-pattern. This assumption is reasonable, as Stern and Gerlach noted the difficulty in developing the detector film since the deposited silver was too thin to see with the naked eye, requiring long irradiation times (eight hours) [2, 33]. Anecdotally, the silver atoms deposited on the detector remained invisible until Gerlach, after smoking a *bad cigar*, accidentally breathed on the film [33]. This reaction, converting the sparse silver atoms (approximately one layer at 10^{16} atoms/cm^2) to silver sulfide, may have introduced a thresholding effect in the visibility of silver

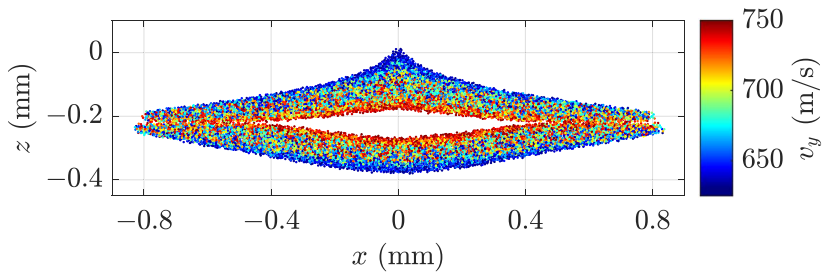

Figure 7. End-pattern for an ensemble of atoms colored according to their initial speeds in the y direction, v_y.

sulfide crystal structures. Furthermore, several other factors in the experiment or photograph processing not modeled here may have led to binarization. Since the locations on the detector and the deposited atom densities are correlated closely with the speeds of the silver atoms, we apply speeds within the chosen upper and lower limits. Selecting $v_{max} = 750$ m/s and $v_{min} = 625$ m/s yields a simulated $a_{sim} = 0.11$ mm and $b_{sim} = 0.2$ mm, which is in good accordance with the above-mentioned modified Maxwellian speed distribution. In reference to figures 1(c)–(d), the SGE reports the width of the pattern at its widest point in zero-field conditions as 0.10 mm, which is consistent with our simulation [2].

For a given propagation speed, there is an associated pattern with a given splitting distance. Lower speeds yield longer flight time to interact with the magnets, thus splitting more. As a result, the final shape is an accumulation of these sub-patterns following the speed distribution. The end-pattern associated with atoms traveling at speeds in the range between v_{min} and v_{max} are shown in figure 7. Distinct color bands are seen for the given speeds, where the overlap is explained due to the initial angular distribution of velocities.

In figure 1, the simulated pattern's length L_{sim}, exceeds that of the experimental pattern, with $L_{sim}/L_{exp} \approx 1.55$. The length of the pattern is determined by the initial angular distribution of velocities and divergence from a collimated beam. In our simulation, the angular distribution and the divergence are governed by the geometries of O, A1, and A2. However, to explain this discrepancy, the historical pictures of the full SG apparatus are helpful, showing a series of uncharacterized slits and apertures between O and A1 (see [14, 25]). These additional apertures reduce the angular deviations and shorten the length of the pattern. In support of this assumption, we placed a third aperture to test the effect of additional collimators and observed a reduced length matching the experimental length while maintaining the shape of the pattern. Because additional apertures are not detailed in the SGE papers, we omitted them for the final pattern.

4. Conclusion

In summary, we modeled the SGE based on the properties, dimensions, and geometries from the historical papers and subsequent review studies. The field properties are calculated using the COMSOL Multiphysics[â] finite element analysis tool. We obtained a magnetic field and gradient agreeing with experimentally reported values. Using this field, we employed a Monte Carlo method to model the atomic trajectories and generated the end-pattern. To the best of our knowledge, the simulations of the magnetic field and the resulting end-pattern represent the most accurate numerical descriptions of the original SGE to date.

Acknowledgments

We would like to thank D. C. Garrett, Z. He, and A. Bengtsson for their insights when discussing this work. This project has been made possible in part by grant number 2020-225832 from the Chan Zuckerberg Initiative DAF, an advised fund of the Silicon Valley Community Foundation.

Data availability statement

All data that support the findings of this study are included within the article (and any supplementary files).

Appendix A End-pattern without quantization

When the magnetic moment of the valence electron of the silver atom is not considered quantized, the expected observation on the detection plate is shown in figure A.1. No splitting is observed.

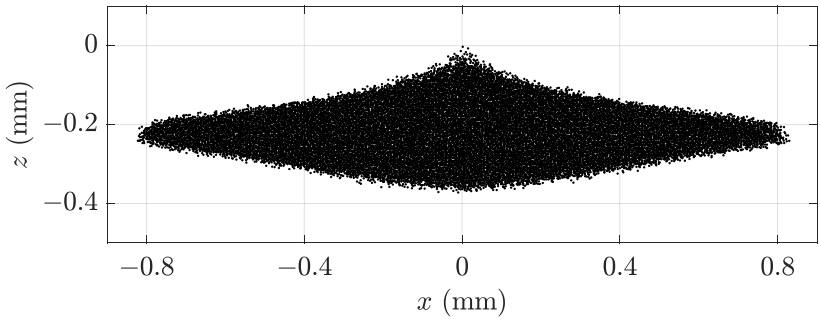

Figure A.1. Classical end-pattern for an ensemble of atoms with a non-quantized magnetic moment sampled from an isotropic distribution.

Appendix B End-pattern with adiabatic spin rotation

When the magnetic moment is assumed to adiabatically rotate following the local field direction, the expected pattern, shown in figure B.1, closely resembles the pattern observed when the magnetic moment is fixed parallel or antiparallel to the z-direction. In other words, the trajectories are minimally altered in regions where the direction of the field deviates from z.

For individual atoms, the change in the final position due to adiabatic spin rotation have been calculated. On average, the final positions approximately shift 10 μm in the x-direction and 3 μm in the z-direction, resulting in only minor differences in the pattern of the scale of hundreds of micrometers. Hence, assuming that the magnetic moment vectors remain fixed along the z-direction is reasonable.

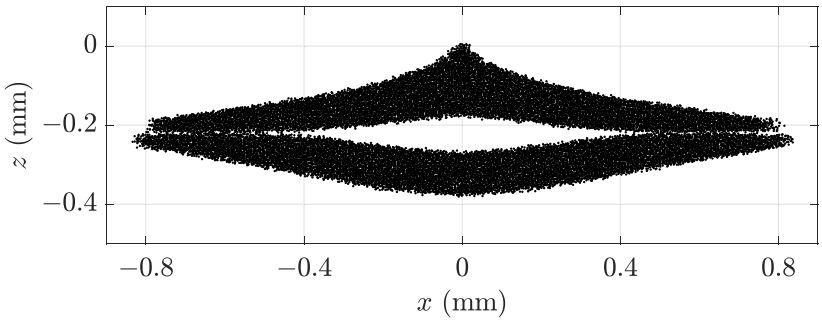

Figure B.1. End-pattern for an ensemble of atoms, assuming the magnetic moment adiabatically follows the local field direction.

ORCID iDs

S Süleyman Kahraman https://orcid.org/0000-0001-8154-367X
Kelvin Titimbo https://orcid.org/0000-0002-4700-3482
Lihong V Wang https://orcid.org/0000-0001-9783-4383

References

[1] Gerlach W and Stern O 1922 Der experimentelle nachweis des magnetischen moments des silberatoms *Z. Phys.* **8** 110
[2] Gerlach W and Stern O 1922 Der experimentelle nachweis der richtungsquantelung im magnetfeld *Z. Phys.* **9** 349
[3] Gerlach W and Stern O 1922 Das magnetische moment des silberatoms *Z. Phys.* **9** 353

[4] Stern O 1920 Eine direkte messung der thermischen molekulargeschwindigkeit *Z. Phys.* **2** 49 56
[5] Stern O 1920 Nachtrag zu meiner arbeit: Eine direkte messung der thermischen molekulargeschwindigkeit *Z. Phys.* **3** 417 421
[6] Sommerfeld A 1916 Zur theorie des Zeeman effekts der wasserstofflinien, mit einem anhang uber den Stark-effekt *Phys. Zs.* **17** 491
[7] Debye P 1916 Quantenhypothese und Zeeman-effekt *Phys. Zs.* **17** 507
[8] Uhlenbeck G E and Goudsmit S 1926 Spinning electrons and the structure of spectra *Nature* **117** 264
[9] Einstein A and Ehrenfest P 1922 Quantentheoretische bemerkungen zum experiment von Stern und Gerlach *Z. Phys.* **11** 31 34
[10] Schmidt-Böcking H, Schmidt L, Lüdde H J, Trageser W, Templeton A and Sauer T 2016 The Stern–Gerlach experiment revisited *Eur. Phys. J.* H **41** 327 364
[11] Sakurai J J and Napolitano J 2011 *Modern Quantum Mechanics* (Cambridge University Press)
[12] Feynman R P 2011 *Feynman Lectures on Physics* IIIQuantum Mechanics(Basic Books)
[13] Messiah A 2014 *Quantum Mechanics* (Dover Publications)
[14] Trageser W 2022 *Der Stern–Gerlach-Versuch* (Springer)
[15] Hsu B C, Berrondo M and Van Huele J-F S 2011 Stern–Gerlach dynamics with quantum propagators *Phys. Rev.* A **83** 012109
[16] De Raedt H, Jin F and Michielsen K 2022 Classical, quantum and event-by-event simulation of a Stern–Gerlach experiment with neutrons *Entropy* **24** 1143
[17] Potel G, Barranco F, Cruz-Barrios S and Gómez-Camacho J 2005 Quantum mechanical description of Stern–Gerlach experiments *Phys. Rev.* A **71** 052106
[18] Das G and Bhattacharyya R 2024 Irreversibility of a Stern-Gerlach experiment *Phys. Rev.* A **110** 062211
[19] Dìaz Bulnes J and Oliveira I 2001 Construction of exact solutions for the Stern-Gerlach effect *Braz. J. Phys.* **31** 488
[20] Alstrøm P, Hjorth P and Mattuck R 1982 Paradox in the classical treatment of the Stern–Gerlach experiment *Am. J. Phys.* **50** 697 698
[21] Home D, Pan A K, Ali M M and Majumdar A S 2007 Aspects of nonideal Stern–Gerlach experiment and testable ramifications *J. Phys. A: Math. Theor.* **40** 13975
[22] Platt D E 1992 A modern analysis of the Stern–Gerlach experiment *Am. J. Phys.* **60** 306
[23] Wennerström H and Westlund P O 2012 The Stern–Gerlach experiment and the effects of spin relaxation *Phys. Chem. Chem. Phys.* **14** 1677
[24] Rashkovskiy S A 2022 Phenomenological theory of the Stern–Gerlach experiment Preprints, 2022100478
[25] Gerlach W and Stern O 1924 Über die richtungsquantelung im magnetfeld *Ann. Phys.* **379** 673
[26] Gerlach W 1925 Über die Richtungsquantelung im Magnetfeld II. Experimentelle Untersuchungen über das Verhalten normaler Atome unter magnetischer Kraftwirkung *Ann. Phys.* **381** 163
[27] 1998 *COMSOL Multiphysics*^{a} *v. 5.4.* www.comsol.com comsol ab, Stockholm, Sweden
[28] Lucas C B 2014 *Atomic and Molecular Beams: Production and Collimation* (CRC Press)
[29] Mostafaeipour F, Titimbo K, Kahraman S S and Wang L V (2023) Simulation of atom trajectories in the original Stern–Gerlach experiment *https://github.com/coilcqd/SternGerlachAtomicTrajectory*
[30] Devereux M 2015 Reduction of the atomic wavefunction in the Stern–Gerlach magnetic field *Can. J. Phys.* **93** 1382
[31] Rumble J R, Bruno T J and Doa M J 2022 *CRC Handbook of Chemistry and Physics: A ready-reference Book of Chemical and Physical Data, 103rd ed* (CRC Press)
[32] Ramsey N 2005 *Molecular Beams* (Clarendon Press)
[33] Friedrich B and Herschbach D 2003 Stern and Gerlach: how a bad cigar helped reorient atomic physics *Phys. Today* **56** 53 59